

An Improved PLL for PMSM Sensorless Control in Estimated Coordinate

Li Helin^{1,2} and Fazilah Hassan^{1*}

¹Faculty of Electrical Engineering, Universiti Teknologi Malaysia, 81310 UTM Skudai, Johor, Malaysia.

²Faculty of Mechanical and Electrical Engineering, Sichuan Vocational and Technical University of Communications, Sichuan, China.

*Corresponding author: fazilah.hassan@utm.my

Abstract: Permanent magnet synchronous motor (PMSM) uses the permanent magnet in the rotor for excitation. Its high efficiency and controllable power factor make it suitable for electric vehicles and other applications requiring high performance. Numerous studies have explored control strategies for PMSM, and sensorless control in PMSM eliminates the need for a position sensor, thereby reducing system complexity. However, sensorless control systems based on position error are prone to significant transient errors during the speed ramp stage. Typically, with a third-order actual position at a given ramp speed, the traditional type-II quadrature PLL (QPLL) is unable to estimate the position without incurring static error. This paper proposes an improved type III phase-locked loop (IPLL), which can effectively reduce this error, easier parameters tuning, and be suitable for all sensorless control based on position error. A detailed theoretical analysis and simulation comparison of sensorless systems based on QPLL and IPLL are presented. Simulation results verified that the proposed IPLL has stronger suppression ability to error and can limit the maximum position error to less than 3° , resulting in stronger load-carrying performance.

Keywords: permanent magnet synchronous motor (PMSM), sensorless control, estimated rotating coordinate, improved phase-locked loop (IPLL), estimate state observer (ESO)

© 2025 Penerbit UTM Press. All rights reserved

Article History: received 8 December 2024; accepted 13 March 2025; published 30 April 2025

1. INTRODUCTION

Permanent magnet synchronous motors (PMSMs) are commonly utilized in applications such as electric vehicles, robotics, and household appliances owing to their high-power density, efficiency, straightforward design, and accessible field-weakening capabilities [1]. The rotor of a PMSM contains permanent magnets, while the stator windings are arranged in distributed slots. This adds to the system's cost, size, and operational inertia, while diminishing its robustness. Consequently, sensorless control strategies for PMSMs can address these drawbacks. Precise rotor position estimation is particularly critical in sensorless control systems for PMSMs, as it reduces costs, lowers system complexity, and improves overall robustness [2-3].

Currently, the primary methods to achieve sensorless motor control are model-based and signal injection approaches, which are applicable to medium-high and zero-low speed ranges, respectively. When the speed is quite low, usually 10% of the rated speed, the motor's back electromotive force (EMF) is small, which is difficult to be accurately estimate, as well as the low signal-to-noise ratio, especially at zero speed, the estimation system based on the model method has no available signals. Especially at zero speed, the model-based estimation system lacks usable signals. At this time, injecting an appropriate signal is necessary. High-frequency square wave signals have

been proposed widely in many studies due to their simplicity and ease of digital implementation. However, the injection of additional signals can lead to issues such as torque ripple, audible noise, system delays, and reduced control accuracy [4-6]. Furthermore, the signal injection method relies on motor saliency. When the anisotropy ratio is below 1.2, particularly in surface-mounted PMSMs, closed-loop control becomes difficult to achieve using signal injection [7].

It is more challenging to adapt sensorless control in zero-low speed range than medium-high speed range. In the model-based approach, parameters such as EMF, extended EMF (EEMF), and flux linkage are commonly used as estimation variables [8]. The estimation strategies include direct calculation method, observer method and intelligent control estimation method [2,3,9]. The algorithm can be implemented in $\alpha\beta$ and $\gamma\delta$ frame. The spatial relations of several coordinates are shown in Figure 1, where abc is the three-phase stationary coordinate, $\alpha\beta$ is the two-phase stationary coordinate ($\alpha\beta$ frame), dq is the two-phase real rotating coordinate, and $\gamma\delta$ is the two-phase estimated rotating coordinate ($\gamma\delta$ frame). The corresponding rotor position information can be obtained from the currents in $\alpha\beta$ and $\gamma\delta$ reference frames, and the voltage information is also required for the medium-high speed algorithm, as shown in Figure 2. Generally, position estimation in the $\alpha\beta$ frame is based on the sine and cosine

information of actual rotor position. This makes closed-loop operation simple but with relatively poor anti-interference capability. The $\gamma\delta$ -frame estimation is based on position error with naturally closed loop property, providing high immunity to interference, although the closed-loop operation is relatively complex [8,10]. This paper focuses on the model-based method to improve the estimation accuracy, and anti-interference and broaden the low-speed domain [11-15].

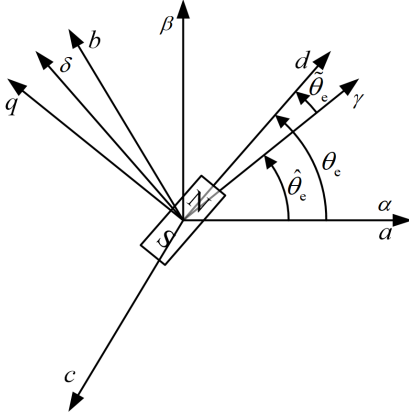


Figure 1. Spatial relations of several coordinates

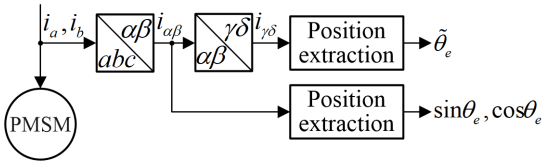


Figure 2. Position information extraction in $\gamma\delta$ or $\alpha\beta$ frames

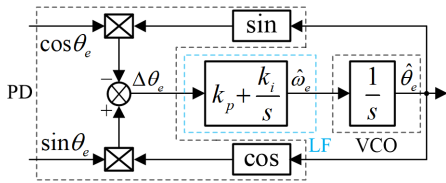


Figure 3. QPLL processes the position signal extracted from the $\alpha\beta$ frame

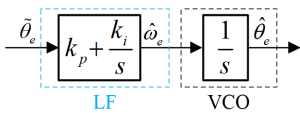


Figure 4. QPLL processes the position error signal extracted from the $\gamma\delta$ frame

The phase-locked loop (PLL) is a crucial component in sensorless control. Its performance is directly related to the accuracy of the estimated speed and position. PLL consists of phase detector (PD), loop filter (LF) and voltage-controlled oscillator (VCO). The function of PD is to obtain the equivalent position error between the input

signal and the output signal. The frequency of the PLL's output is acquired by LF, and the phase angle of the output signal is captured in VCO by integrating the. Once the frequency of the output signal tracks the frequency of the input signal, the phase error will eventually converge to zero, and the PLL completes the phase-locked function. In the $\alpha\beta$ frame, position-based quadrature PLL(QPLL) needs to construct the position error signal by heterodyne method, as illustrated in Figure 3. For the QPLL based on position error, the position error signal obtained in Figure 2 can be directly input, and its structure is relatively simpler. The traditional QPLL exhibits significant errors during ramp acceleration and deceleration stages. Numerous studies have examined the removal of the transient errors in the $\alpha\beta$ frame, where the estimated position is directly obtained [16-17]. However, there are few literature studies on how to eliminate this error in the $\gamma\delta$ frame, which is based on position error. It is important to note that most signal injection methods are based on position error, and estimation based on position error offers stronger anti-interference and robustness. The research on this issue has more practical significance. Furthermore, among model-based methods, the sliding mode observer (SMO) is the most extensively studied. However, to mitigate chattering, most literature employs continuous functions in place of the sign function [8,18-19], high-order SMO and parameter adaptive SMO [13, 20-21]. Chattering is the essential representative of sliding mode control. The greater the chattering, the better the anti-interference capability, and vice versa. Considering the algorithm complexity, observer parameter adaptability, and system performance, this paper employs an extended state observer to estimate the back EMF in the $\gamma\delta$ frame, obtain the position error, and subsequently study and improve the performance of the PLL.

The main contributions of the work are as follows.

1. An improved type III PLL is proposed for estimation systems based on position error, effectively eliminating transient errors within the stage of given ramp speed ramp and suitable for all sensorless control based on position error.
2. The detailed parameter selection of IPLLL is given, and the performance comparison between QPLL and IPLLL is verified by simulation.

2. ESTIMATING EEMF BY ESO IN $\gamma\delta$ FRAME

2.1 Model of Permanent Magnet Synchronous Motor

In the estimated rotational reference $\gamma\delta$ frame, the mathematical model of the PMSM can be described as follows.

$$\begin{bmatrix} u_\gamma \\ u_\delta \end{bmatrix} = \begin{bmatrix} R_s + pL_d & -\omega_e L_q \\ \omega_e L_q & R_s + pL_d \end{bmatrix} \begin{bmatrix} i_\gamma \\ i_\delta \end{bmatrix} - \begin{bmatrix} E_\gamma \\ E_\delta \end{bmatrix} \quad (1)$$

$$\begin{bmatrix} E_\gamma \\ E_\delta \end{bmatrix} = E_{ex} \begin{bmatrix} \sin \tilde{\theta}_e \\ -\cos \tilde{\theta}_e \end{bmatrix} + (\omega_e - \hat{\omega}_e) L_d \begin{bmatrix} -i_\delta \\ i_\gamma \end{bmatrix} \quad (2)$$

$$E_{ex} = (L_d - L_q)(\omega_e i_d - p i_q) + \omega_e \psi_f \quad (3)$$

Here, u_γ , u_δ , i_γ , i_δ , E_γ , E_δ denote the terminal voltages, currents, and extended back EMF along the γ -axis and δ -axis, respectively. The term E_{ex} corresponds to the amplitude of EEMF. Parameters R_s and ψ_f represent the phase resistance and the flux linkage of the permanent magnet. Similarly, L_d and L_q are the inductances along the d -axis and q -axis, while i_d and i_q indicate the respective currents. The actual and estimated electrical angular velocities of the rotor are symbolized by ω_e and $\hat{\omega}_e$, while θ_e and $\hat{\theta}_e$ refer to the actual and estimated rotor positions, $\tilde{\theta}_e = \theta_e - \hat{\theta}_e$. Lastly, p represents the differential operator.

As observed from Equation (2), the components E_γ and E_δ include information related to the position error. Using an appropriate estimator, it is possible to derive the estimated speed and position from this information. Once the system reaches a stable state, $\omega_e \approx \hat{\omega}_e$, the estimation error becomes negligible.

2.2 Estimating Extend Back Electromotive Force by Linear Estimate State Observer

In Equation (1), by treating E_γ and E_δ as external disturbances, a straightforward second-order linear extended state equation (LESEQ) can be formulated. This equation can be expressed in a unified form as follows.

$$\begin{cases} e_{\gamma,\delta} = \hat{i}_{\gamma,\delta} - i_{\gamma,\delta} \\ \frac{d\hat{i}_{\gamma,\delta}}{dt} = \frac{1}{L_d}(u_{\gamma,\delta} - R_s i_{\gamma,\delta} \pm \omega_e L_q i_{\delta,\gamma} + \hat{E}_{\gamma,\delta}) - \beta_{\gamma,\delta 1} e_{\gamma,\delta} \\ \dot{\hat{E}}_{\gamma,\delta} = -\beta_{\gamma,\delta 2} e_{\gamma,\delta} \end{cases} \quad (4)$$

Here, $\hat{i}_{\gamma,\delta}$, $\hat{E}_{\gamma,\delta}$ are the estimated values of i_γ , i_δ , E_γ , E_δ . $e_{\gamma,\delta}$ is the current error. $\beta_{\gamma,\delta 1}$, $\beta_{\gamma,\delta 2}$ are the feedback coefficient, which are positive constants greater than zero.

To guarantee the stable convergence of the linear extended state observer (LESO), the stability conditions are briefly derived using the δ -axis LESEQ as an example, the detailed derivation can be referred to [12]. By assuming constant motor parameters, the equations (1) and (4) are transformed into discrete-time form through the application of the Euler approximation.

$$i_\delta(k+1) = i_\delta(k) + t_s [u_\delta(k) - R_s i_\delta(k) - \omega_e L_q i_\gamma + E_\delta(k)] / L_d \quad (5)$$

$$\begin{cases} \hat{i}_\delta(k+1) = \hat{i}_\delta(k) + t_s [u_\delta(k) - R_s i_\delta(k) - \omega_e L_q i_\gamma + \hat{E}_\delta(k)] / L_d \\ \quad - t_s \beta_{\delta 1} [\hat{i}_\delta(k) - i_\delta(k)] \\ \hat{E}_\delta(k+1) = \hat{E}_\delta(k) - t_s \beta_{\delta 2} [\hat{i}_\delta(k) - i_\delta(k)] \end{cases} \quad (6)$$

where t_s is the sampling period of the system.

Let $e_\delta(k) = \hat{i}_\delta(k) - i_\delta(k)$, $\eta_\delta(k) = \hat{E}_\delta(k) - E_\delta(k)$, and by subtracting equation (5) from (6), the result can be directly written in matrix form as

$$\begin{bmatrix} e_\delta(k+1) \\ \eta_\delta(k+1) \end{bmatrix} = \underbrace{\begin{bmatrix} 1 - t_s \beta_{\delta 1} & t_s / L_d \\ -t_s \beta_{\delta 2} & 1 \end{bmatrix}}_A \begin{bmatrix} e_\delta(k) \\ \eta_\delta(k) \end{bmatrix} - \begin{bmatrix} 0 \\ E_\delta(k+1) - E_\delta(k) \end{bmatrix} \quad (7)$$

To guarantee the designed LESO achieves stable convergence, the placement of the eigenvalues of the coefficient matrix A plays a critical role. Based on control theory, the eigenvalues must remain confined within the unit circle in the complex plane. To further enhance system robustness and minimize potential oscillatory behavior, a pole-placement strategy is adopted, where both poles are assigned to $z = -\beta_\delta$, satisfying the condition $-1 < \beta_\delta < 1$. The $\beta_{\delta 1,2}$ can be solved from (8), that is (9).

$$|zI - A| = \begin{vmatrix} z - 1 + t_s \beta_{\delta 1} & -t_s / L_d \\ t_s \beta_{\delta 2} & z - 1 \end{vmatrix} = (z - \beta_\delta)^2 \quad (8)$$

$$\beta_{\delta 1} = \frac{2(1 - \beta_\delta)}{t_s}, \beta_{\delta 2} = \left(\frac{1 - \beta_\delta}{t_s}\right)^2 L_d \quad (9)$$

Let $\beta = (1 - \beta_\delta) / t_s$, where the condition $-1 < \beta_\delta < 1$ holds. Under this constraint, Equation (9) can be reformulated into a simplified expression, as shown below

$$\beta_{\delta 1} = 2\beta, \beta_{\delta 2} = \beta^2 L_d, 0 < \beta < 2 / t_s \quad (10)$$

where β is the designed bandwidth of LESO.

From [22], it is recommended to set $\beta_{\delta 1} = 1 / t_s$, which corresponds to a bandwidth β of 5000.

The selection of the bandwidth and stability conditions for the γ -axis LESEQ follow the same principles as those applied to the δ -axis. As derived from equation (7), when the current error $e_{\gamma,\delta}$ is eliminated, accurate estimations of E_γ and E_δ can be achieved. Then the estimated position error can be obtained.

Based on LESO, a linear active disturbance rejection controller (LADRC) is designed, incorporating a direct linear feedback mechanism for the current error [22]. In contrast to the traditional PI controller, which necessitates tuning two separate parameters, LADRC streamlines this process by relying on a single tuning parameter, K_{ADRC} , to define its performance.

3. POSITION ESTIMATION WITH PHASE-LOCKED LOOP

3.1 Traditional QPLL

Referring to Figure 4, the transfer function about the rotor position estimation error to the actual position can be obtained, that is

$$\frac{\tilde{\theta}_e}{\theta_e} = \frac{1}{1 + \hat{\theta}_e / \tilde{\theta}_e} \approx \frac{s^2}{s^2 + k_p s + k_i} \quad (11)$$

In (11), when the position error is very small, $\Delta \theta_e \approx \tilde{\theta}_e$.

When the reference speed follows a ramp profile, the actual rotor position, θ_e , can be expressed as

$$\theta_e = \frac{a}{s^3} \quad (12)$$

Here, a represents the slope of the given electrical angular velocity, expressed in radians per second squared (rad/s^2).

By combining equations (11) and (12) and applying the final value theorem, the position estimation error, as the system approaches stability, can be determined as follows

$$\tilde{\theta}_e|_{t \rightarrow +\infty} = \lim_{s \rightarrow 0} \frac{s^2}{s^2 + k_p s + k_i} \cdot \frac{a}{s^3} \cdot s = \frac{a}{k_i} \quad (13)$$

From equation (13), it is evident that when the reference speed follows a ramp profile, an estimated error in the position always exists. To reduce this error, the integral gain k_i of the PLL can be increased, or the slope of the given speed can be decreased. Here, k_i represents the integral gain, which helps eliminate steady-state error by addressing accumulated position errors. However, excessively large k_i may introduce noise and oscillations.

In most practical applications, the acceleration a is relatively fixed. The $\tilde{\theta}_e$ is inversely proportional to k_i , but as k_i increases beyond a certain point, the reduction in error becomes minimal, and excessive k_i degrades system stability.

3.2 Proposed IPLL and Parameters Setting

From equation (13), to ensure that the estimated error $\tilde{\theta}_e$ becomes zero, the numerator of the PLL transfer function should be at least s^3 . Under this condition, the PLL transfer function can be expressed as

$$\frac{\tilde{\theta}_e}{\theta_e} = \frac{s^3}{s^3 + As^2 + Bs + C} \quad (14)$$

where A , B and C are constants to be determined.

According to equation (14), the open-loop transfer function from $\tilde{\theta}_e$ to $\hat{\theta}_e$ can be calculated backwards in equation (15).

$$\frac{\hat{\theta}_e}{\tilde{\theta}_e} = \frac{\theta_e - \tilde{\theta}_e}{\tilde{\theta}_e} = \frac{As^2 + Bs + C}{s^3} \approx \frac{\hat{\theta}_e}{\Delta\theta_e} \quad (15)$$

Equation (15) represents a type III system. To distinguish it from traditional QPLL, we abbreviate it as IPLL. To achieve improved stability margins, the system is configured as follows

$$\frac{\hat{\theta}_e}{\Delta\theta_e} = K \frac{(s + \omega_z)^2}{s^3} \quad (16)$$

where K is the open-loop gain of the system and $-\omega_z$ is its zero point.

The phase margin (PM) of open-loop transfer function corresponding for equation (16) can be expressed as

$$PM = 2\text{atan} \frac{\omega_c}{\omega_z} - \frac{\pi}{2} \quad (17)$$

where ω_c is the cutoff frequency, satisfying

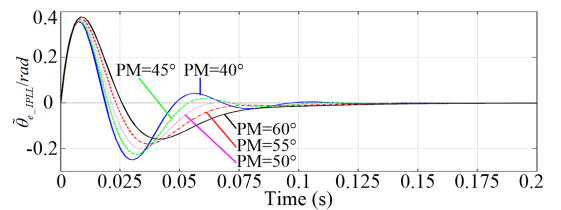
$$\omega_c = \frac{K}{\sin^2(2\text{atan} \frac{\omega_c}{\omega_z})} \quad (18)$$

Combining equations (17) and (18), K , ω_z can be expressed as PM and ω_c with

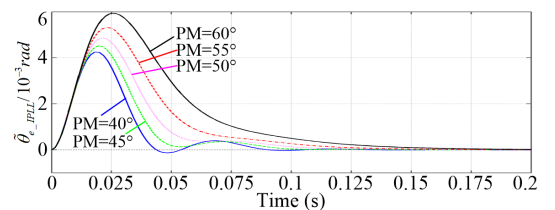
$$\omega_z = \frac{\omega_c}{\tan(\text{PM}) + \sec(\text{PM})} \quad (19)$$

$$K = \omega_c \frac{\sin(\text{PM}) + 1}{2} \quad (20)$$

From equations (19) and (20), the parameter tuning of IPLL can be realized as long as PM and ω_c are determined. In control engineering, the PM is typically set between 40° and 60° based on practical experience. This range provides a good balance between stability and responsiveness, reducing the risk of excessive oscillations while ensuring the system reacts effectively to dynamic changes. Figure 5 illustrates the transient response curves of the rotor position estimation error for various PM at a fixed cutoff frequency of $\omega_c = 175 \text{ rad/s}$. This curve is obtained from the inverse Laplace transform of equation (14), with the constants of the step function and ramp function set to 100. A smaller PM enhances the dynamic performance in tracking the rotor position but leads to prolonged oscillation. Conversely, a larger PM reduces oscillations, resulting in over-damping and longer convergence times. Figure 6 presents the magnitude frequency characteristics of IPLL under different PMs. A lower PM results in a higher amplification gain for the closed-loop transfer function in equation (14), leading to more pronounced oscillations in the transient response of IPLL. The same conclusion can be drawn as in Figure 5. For satisfactory dynamic performance, this study recommends selecting a PM within the range of 45° to 50° .



(a)



(b)

Figure 5. Transient response of the rotor position error with various PM. (a) Speed step input. (b) Speed ramp input

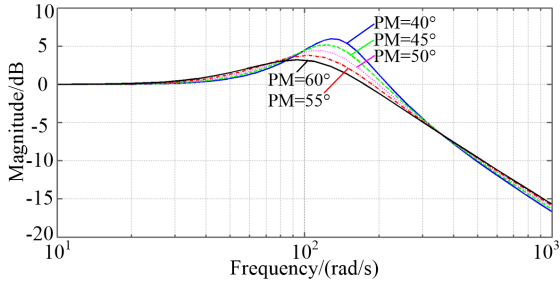
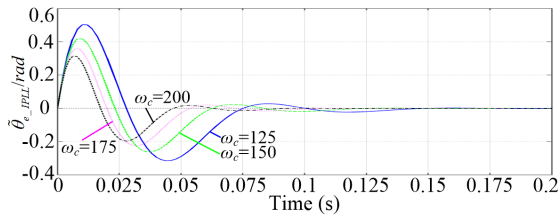


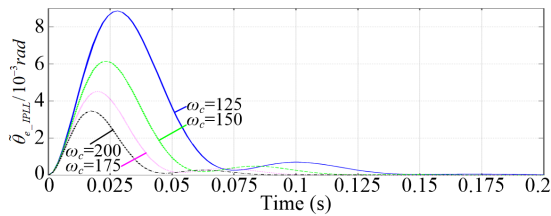
Figure 6. Magnitude-frequency characteristic of IPLLL under different PM

Figure 7 illustrates the transient response curves of rotor position error for various cutoff frequencies (ω_c) with a fixed phase margin (PM=45°). A smaller ω_c results in reduced dynamic performance in rotor position tracking, while a larger ω_c enhances dynamic performance and shortens convergence time.

Figure 8 presents the Bode diagrams of IPLLL under different ω_c values. A smaller ω_c provides stronger noise suppression but at the cost of slower dynamic response. Conversely, increasing ω_c improves dynamic performance but reduces noise suppression in the mid-frequency range. Therefore, the selection of ω_c should carefully balance dynamic performance and noise suppression capabilities.



(a)



(b)

Figure 7. Transient response of the rotor position error with various ω_c . (a) speed step input. (b) speed ramp input

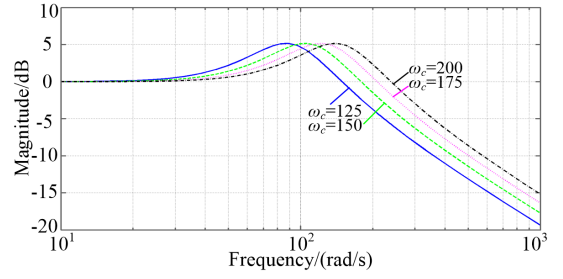


Figure 8. PM Bode diagram of IPLLL under different ω_c

Additionally, for equation (16), the transfer function from $\Delta\theta_e$ to the estimated speed can be derived through transformation, as follows

$$\frac{\hat{\omega}_e}{\Delta\theta_e} = K \frac{(s + \omega_z)^2}{s^2} = (\sqrt{K} + \frac{\omega_z \sqrt{K}}{s})^2 \quad (21)$$

From equation (21), the loop filter (LF) of the IPLLL is functionally equivalent to two proportional-integral (PI) controllers with identical parameters connected in series, as illustrated in Figure 9. This configuration differs from the loop filter of the QPLL, which consists of a single PI controller. The additional PI in the IPLLL enhances its ability to handle higher-order dynamics and improves its tracking accuracy for rotor position, particularly under rapidly changing conditions.

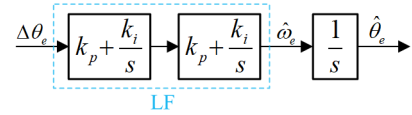


Figure 9. Diagram of proposed IPLLL

4. SIMULATION VERIFICATION RESULTS

Based on the above discussion, the block diagram of the sensorless control system employing IPLLL in the $\gamma\delta$ reference frame is illustrated in Figure 10. In this diagram, p_n represents the number of pole pairs of the motor. The estimated speed from the IPLLL is utilized by both the speed regulator and the estimated EEMF, while the estimated rotor position is employed for coordinate transformations.

Using Figure 10 as a reference, a corresponding Simulink model is developed. The key parameters of the PMSM and the system configuration are summarized in Table 1. The hardware parameters of the motor and inverter are derived from real experimental platform in Table 1. The PMSM is a servo motor, and the parameters are provided by the manufacturer. The IPLLL parameters are derived from the simulation analysis in Section 3.2. Due to the different structures between QPLL and IPLLL, in order to maintain fairness in comparison, both adopt comparable open-loop gains, around 150, which is derived from PM and ω_c through equation (20).

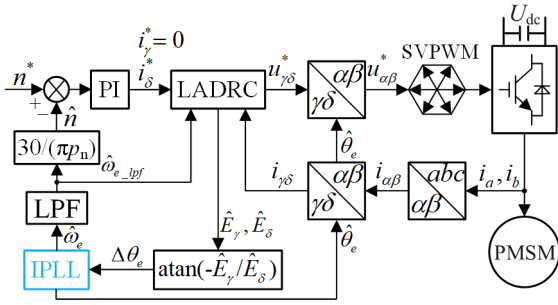


Figure 10. Diagram of PMSM sensorless drive adopting IPLL in $\gamma\delta$ reference frame

Table 1. Main parameters of PMSM test platform

Parameter	Value
Rated power	750W
Rated torque	2.4N.m
Rated speed	3000r/min
Stator resistance	1.45 Ω
PM flux linkage	0.12Wb
Inductance(L_d/L_q)	6.04/9.06mH
Pole pairs	5
DC-link voltage	311V
Sampling frequency	10kHz
PWM carrier frequency	10kHz
PM/ ω_c	45 $^\circ$ /175rad/s
k_p, k_i for IPLL in (21)	12.2/885
k_p, k_i for QPLL	150/5625
Bandwidth of LESO(β)	5000
K_{ADRC} for γ axis ACR	90
K_{ADRC} for δ axis ACR	110

The simulated operating situations are starting with a step at 300rpm without load by using the inertia of the rotor at the initial moment, loading suddenly rated load at 2s, accelerating to 1800rpm with rated load and 900rpm/s at 4s, decelerating to 300rpm with rated load and 900rpm/s at 9s and unloading suddenly rated load at 12s.

Figure 11 shows the input signals of QPLL and IPLL. Although QPLL has reached a steady state, there is still a static error in the input signal within the stage of acceleration and deceleration in ramp. In the estimation system adopting IPLL, this input signal can be quickly limited to near 0. Figure 11 and Figure 12 have a high degree of similarity.

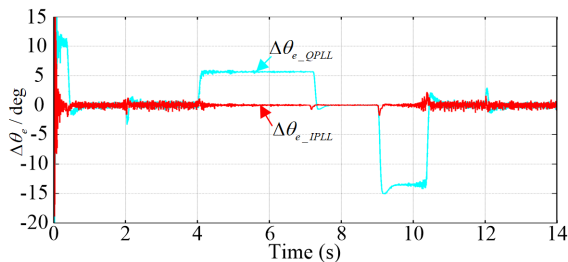


Figure 11. Signals input to the PLL

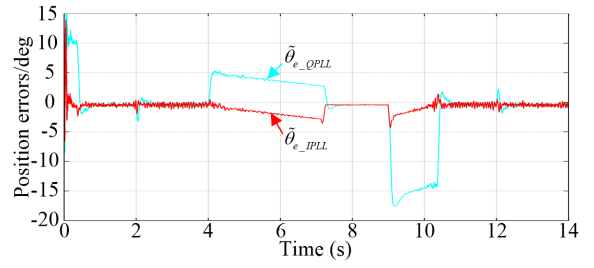


Figure 12. Position errors using QPLL and IPLL

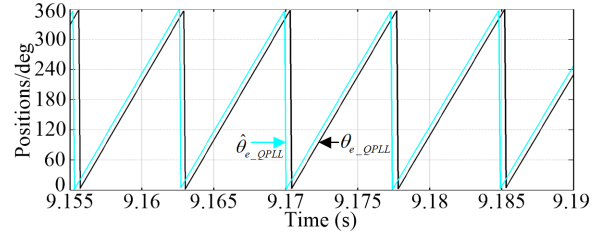


Figure 13. Real and estimated positions using QPLL

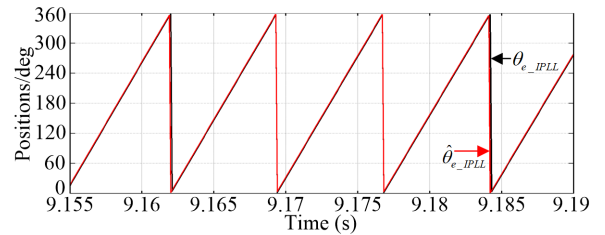
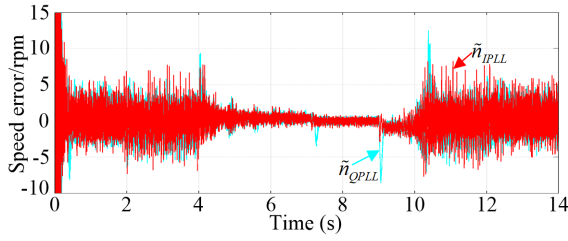


Figure 14. Real and estimated positions using IPLL

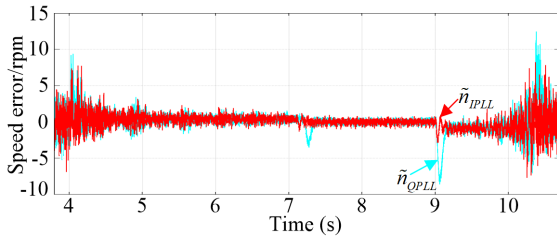
Figure 12 shows the position estimation errors obtained by the traditional QPLL and the proposed IPLL under the above operating situations. Obviously, during the stage of given ramp speed and sudden load changes, IPLL can significantly reduce estimation errors compared to QPLL. In order to show this difference more clearly, Figure 13 and Figure 14 gives the respective position signals within 9.155-9.19s. In Figure 13, a significant position error can be observed, while the two overlap so much that it is difficult to distinguish them in Figure 14.

Note that both QPLL and IPLL have the same error bias, approximately -2.75° , when the speed reaches 1800rpm. During the stages of acceleration and deceleration, the slope of the position error is the same, about $-5 \times 10^{-5} \text{ rad}/(\text{rad}/\text{s})$, which is equivalent to the system sampling frequency, which is mainly caused by sampling errors. Owing to the estimated EEMF having the same amplitude attenuation, when the speed reaches 1800rpm, the position error will fall back to a smaller initial error. Due to the closed-loop estimation based on position error in $\gamma\delta$ frame, the sampling error cannot be simply compensated on the estimated position. This can be verified by Figure 11, which illustrates that the input signals of the PLL have reached a smooth steady state during the corresponding transient stage. Although there is a sampling error, it does not affect the robustness and control accuracy of the

sensorless system.



(a)



(b)

Figure 15. Speed errors using QPLL and IPLL. (a) The display time range is 0-14s. (b) The detailed view of the 4-10s range

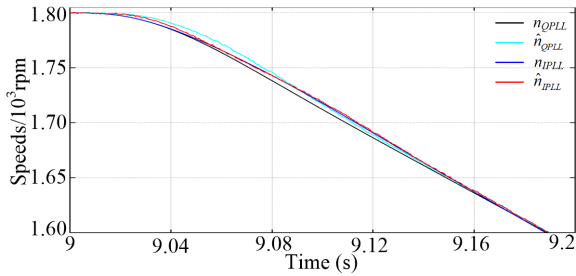


Figure 16. Real and estimated speed using QPLL and IPLL

Figure 15 and Figure 16 show the speed errors of these two estimation systems, and Figure 15(b) expands the 3.8-10.7s time range in Figure 15(a) to more clearly illustrate the differences between the two. When the speed leaves and reaches the steady state, the estimation system using IPLL has smaller speed error and stronger suppression ability to error. There is no obvious difference between the two systems in other conditions, because QPLL and IPLL are both no static errors for the estimated speed.

The δ -axis currents for these two systems are shown in Figure 17. Due to the smaller position error, the IPLL-based sensorless system will reach steady state faster, about 0.1s ahead (15 fundamental cycles corresponding to 1800rpm). When slowing down, the recoil current is less.

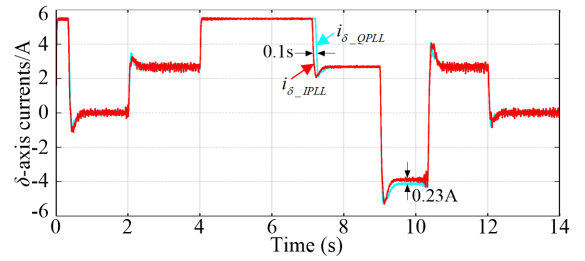


Figure 17. Currents in δ axis using QPLL and IPLL

Table 2 presents the maximum values of these performance indices for the two sensorless systems, providing an overview of their comparison. It can be inferred that IPLL exhibits a relatively strong error suppression capability and helps maintain the error within a very small range.

Table 2. Summary of the Comparison of Maximum Performance Indexes

Comparison items	QPLL	IPLL
Input signals of PLL($\Delta\theta_e$)	-13.5°	2°
Position error ($\tilde{\theta}_e$)	-17.6°	-4.2°
Speed error (\tilde{n})	10rpm	5rpm

5. CONCLUSION

The sensorless control system based on position error exhibits significant transient errors during ramped acceleration and deceleration. This article takes removing this error as the starting point, estimates the EEMF through LESO to obtain the position error, and then analyze the performance of PLL. In the traditional type II QPLL, the actual position is a third-order signal under ramped speed conditions, resulting in a large static error. In contrast, the proposed type III IPLL structure can theoretically reduce transient error to zero. In practice, despite sampling errors, the IPLL reduces errors from over 15° to within 3° , enhancing control accuracy, load capacity, and dynamic performance in sensorless systems. Besides, the parameters selection is given in detail, which simplifies the tedious parameter tuning in QPLL. This IPLL approach is applicable to all estimation systems that use position error as the PLL input.

REFERENCES

- [1] Z. Chen, W. Qu, and J. Qiu, "Ripple excitation-based adaptive sensorless control of IPMSM in full speed range," *IEEE Access*, vol. 11, pp. 33160-33177, Mar. 2023.
- [2] W. Zine, Z. Makni, E. Monmasson, L. Ldkhajine and B. Condamine, "Interests and limits of machine learning-based neural networks for rotor position estimation in EV traction drives," *IEEE Trans. Ind. Inform.*, vol. 14, pp. 1942-1952, May. 2018.
- [3] Q. Abdullah, N. Farah, M. S. Ahmed, N. S. M. Shah and O. Aydogdu, "Sensorless speed control of induction motor drives using reinforcement learning

- and self-tuning simplified fuzzy logic controller,” *IEEE Access.*, vol. xx, pp. 1-1, Jul. 2024.
- [4] S. Chen, W. Ding, X. Wu, L. Huo, and R. Hu “Sensorless control of IPMSM drives using high-frequency pulse voltage injection with random pulse sequence for audible noise reduction,” *IEEE Trans. Power Electron.*, vol. 38, no. 9, pp. 9395-9408, Aug. 2023.
- [5] Y. Zhang, Z. Yin, J. Liu, R. Zhang, and X. Sun, “IPMSM sensorless control using high-frequency voltage injection method with random switching frequency for audible noise improvement,” *IEEE Trans. Ind. Electron.*, vol. 67, no. 7, pp. 6019-6030, Jul. 2020.
- [6] M.-W. Kim, M. Biswas, and J.-W. Park, “New acoustic noise reduction method for signal-injection-based IPMSM sensorless drive,” *IEEE Trans. Power Electron.*, vol. 38, no. 3, pp. 3180-3190, Mar. 2023.
- [7] A. Benevieri, A. Formentini, M. Marchesoni, M. Passalacqua, and L. Vaccaro, “Sensorless control with switching frequency square wave voltage injection for SPMSM with low rotor magnetic anisotropy,” *IEEE Trans. Power Electron.*, vol. 38, no. 8, pp. 10060-10072, Aug. 2023.
- [8] W. He, X. Wu, J. Chen, and Y. Wang, “Comparative study of sensorless control of permanent magnet synchronous motor realised by sliding-mode observer,” *IET Power Electron.*, vol. 3, no. 6, pp. 1191-1199, May. 2020.
- [9] H. Ding, X. Zou, and J. Li, “Sensorless control strategy of permanent magnet synchronous motor based on fuzzy sliding mode observer,” *IEEE Access.*, vol. 10, pp. 36743-36752, Apr. 2022.
- [10] N. Bianchi, S. Bolognani, J.-H. Jang, and S.-K. Sul, “Comparison of PM motor structures and sensorless control techniques for zero-speed rotor position detection,” *IEEE Trans. Power Electron.*, vol. 22, no. 6, pp. 2466-2475, Nov. 2007.
- [11] X. Wu, C. Li, Y. Zhang, and S. Chen, “Sensorless control of IPMSM equipped with LC sinusoidal filter based on full-order sliding mode observer and feedforward QPLL,” *IEEE Trans. Power Electron.*, vol. 39, no. 7, pp. 8072-8085, Jul. 2024.
- [12] F. Jiang, S. Sun, A. Liu, Y. Xu, and Z. Li, “Robustness improvement of model-based sensorless SPMSM drivers based on an adaptive extended state observer and an enhanced quadrature PLL,” *IEEE Trans. Power Electron.*, vol. 36, no. 4, pp. 4802-4814, Apr. 2024.
- [13] D. Liang, J. Li, R. Qu, and W. Kong, “Adaptive second-order sliding-mode observer for PMSM sensorless control considering VSI nonlinearity,” *IEEE Trans. Power Electron.*, vol. 33, no. 10, pp. 8994-9004, Oct. 2018.
- [14] X. Yao, J. Wang, H. Ma, G. Zhang, and Y. Wang, “Improved ROGI-FLL-based sensorless model predictive current control with MRAS parameter identification for SPMSM drives,” *IEEE J. Emerg. Sel. Topics Power Electron.*, vol. 11, no. 2, pp. 1684-1695, Apr. 2023.
- [15] G.-J. Jo and J.-W. Choi, “Rotor flux estimator design with offset extractor for sensorless-driven induction motors,” *IEEE Trans. Power Electron.*, vol. 37, no. 4, pp. 4497-4510, Apr. 2022.
- [16] S. Golestan, M. Monfared, F. D. Freijedo, and M. Guerrero, “Advantages and challenges of a Type-3 PLL,” *IEEE Trans. Power Electron.*, vol. 28, no. 11, pp. 4985-4997, Nov. 2013.
- [17] Z. Novak and M. Novak, “Adaptive PLL-based sensorless control for improved dynamics of high-speed PMSM,” *IEEE Trans. Power Electron.*, vol. 37, no. 9, pp. 10154-10165, Sep. 2022.
- [18] S. Ok, Z. Xu, and D.-H. Lee, “A sensorless speed control of high-speed BLDC motor using variable slope SMO,” *IEEE Trans. Ind. Appl.*, vol. 60, no. 2, pp. 3221-3228, Mar. 2024.
- [19] Y. Zhao, W. Qiao, and L. Wu, “An adaptive quasi-sliding-mode rotor position observer-based sensorless control for interior permanent magnet synchronous machines,” *IEEE Trans. Power Electron.*, vol. 28, no. 12, pp. 5618-5629, Dec. 2013.
- [20] Z. Li, S. Zhou, Y. Xiao, and L. Wang, “Sensorless vector control of permanent magnet synchronous linear motor based on self-adaptive super-twisting sliding mode controller,” *IEEE Access.*, vol. 7, pp. 44998-45011, Apr. 2019.
- [21] Z. Chen, A. A. Dawara, X. Zhang, H. Zhang, and C. Liu, “Adaptive sliding mode observer-based sensorless control for spmsm employing a dual-PLL,” *IEEE Trans. Transp. Electric.*, vol. 8, no. 1, pp. 1267-1277, Mar. 2022.
- [22] J. Han, “From PID to active disturbance rejection control,” *IEEE Trans. Ind. Electron.*, vol. 56, no. 3, pp. 900-906, Mar. 2009.